

RESEARCH ARTICLE

# Numerical Simulation of Dry Granular Flow Impacting a Rigid Wall Using the Discrete Element Method

Fengyuan Wu, Yunyun Fan\*, Li Liang, Chao Wang

Key Laboratory of Ministry of Education on Safe Mining of Deep Metal Mines, Northeastern University, Shenyang, P. R. China

\* [yunyunfan@126.com](mailto:yunyunfan@126.com)



OPEN ACCESS

**Citation:** Wu F, Fan Y, Liang L, Wang C (2016) Numerical Simulation of Dry Granular Flow Impacting a Rigid Wall Using the Discrete Element Method. PLoS ONE 11(8): e0160756. doi:10.1371/journal.pone.0160756

**Editor:** Michael Peters, Virginia Commonwealth University, UNITED STATES

**Received:** April 8, 2016

**Accepted:** July 25, 2016

**Published:** August 11, 2016

**Copyright:** © 2016 Wu et al. This is an open access article distributed under the terms of the [Creative Commons Attribution License](https://creativecommons.org/licenses/by/4.0/), which permits unrestricted use, distribution, and reproduction in any medium, provided the original author and source are credited.

**Data Availability Statement:** All relevant data are within the paper and its Supporting Information files.

**Funding:** This study was supported by the National Natural Science Foundation of China (Grant No. 41201007, 51474048), the Fundamental Research Funds for the Central Universities (N130401003, L1501009), the Opening fund of State Key Laboratory of Geohazard Prevention and Geoenvironment Protection of Chengdu University of Technology (Grant No. Sklgp2012K010) and the Research Fund for General Science Project of Department of Education of Liaoning Province (Grant No. L2013103).

## Abstract

This paper presents a clump model based on Discrete Element Method. The clump model was more close to the real particle than a spherical particle. Numerical simulations of several tests of dry granular flow impacting a rigid wall flowing in an inclined chute have been achieved. Five clump models with different sphericity have been used in the simulations. By comparing the simulation results with the experimental results of normal force on the rigid wall, a clump model with better sphericity was selected to complete the following numerical simulation analysis and discussion. The calculation results of normal force showed good agreement with the experimental results, which verify the effectiveness of the clump model. Then, total normal force and bending moment of the rigid wall and motion process of the granular flow were further analyzed. Finally, comparison analysis of the numerical simulations using the clump model with different grain composition was obtained. By observing normal force on the rigid wall and distribution of particle size at the front of the rigid wall at the final state, the effect of grain composition on the force of the rigid wall has been revealed. It mainly showed that, with the increase of the particle size, the peak force at the retaining wall also increase. The result can provide a basis for the research of relevant disaster and the design of protective structures.

## Introduction

In recent years, the outbreaks of rockfall, landslide and debris flow are more frequent which threat to people and infrastructures seriously [1–3]. In these geological disasters, granular flow is one of the typical forms with the characteristics of high flow velocity, long runout distance, huge impact force and bad temporal predictability [4, 5]. In order to reduce the impact of disasters, retaining walls are often used to prevent granular flows [6]. Therefore, it is significant to better understand the mechanism of granular flow impacting a retaining wall.

Experimental research—the most common method—not only can analyze the development mechanism of granular flows, but also can obtain the influencing factors of flow velocity and accumulation shape. For this purpose, Manzella et al. [7] used gravel and small blocks as the

**Competing Interests:** The authors have declared that no competing interests exist.

tested material to analyze the energy dissipation in the process of sliding down from an inclined board. Inclined chutes have also adopted as the sideways in many experiments [8–11]. Bi et al. [12] revealed complex influences of chutes with different bumpy surface on the velocity and temperature of the granular flows by using two-dimensionally monodisperse disks. Pudasaini et al. [13] performed experiments of dry granular flow impinging an obstructing wall and presented evolution of the height and velocities of both the supercritical and subcritical flows in detail with the granular-PIV measurements on inclined and inclined plus horizontal channel runout. Moreover, granular materials used in experiments were not the same, such as sand [14], ping-pang-ball [15], and glass sphere [16]. Dufresne [17] used coal as avalanche analogue material to study the processes acting well below the surface of a moving rock or debris avalanche during travel over stationary substrate material.

In numerical simulation, granular flows usually can be modeled by either continuum or discrete approaches. In continuous approaches, granular flows have been treated as a Coulomb, or Coulomb-viscoplastic fluid and analyzed by Eulerian forms of continuity and momentum equation [18–23]. In discrete approaches, Discrete Element Method (DEM) as a common numerical method has been widely applied to the simulations of granular flows [24–28]. Numerical verification of laboratory experiments on granular flows down an inclined chute has been presented using DEM [29, 30]. And the force of granular flow impacting rigid obstacles has been further analyzed [31]. Zhou et al. [32] modeled three-dimensional dry granular flows using DEM. The results showed that flow regimes of granular flows can be well identified by combining granular temperature and the Savage number. Utili et al. [33] presented a numerical simulation of dry granular flows generated by the collapse of prismatic columns using DEM in plane strain conditions. Then, energy dissipation of granular flows in dynamic process was analyzed detailedly. Furthermore, combination of DEM and other numerical methods has been carried out, such as DEM-DLM/FD [34], CFD-DEM [35, 36], MFX-DEM [37]. Manzella et al. [38] used DEM and FEM/DEM to simulate small-scale laboratory experiments which better understand some mechanisms and factors of initial block packing and progressive failure.

The aim of this paper is to investigate the law and mechanism of granular flow impacting a rigid wall using DEM. So far, most of the simulations have been carried out using spherical element. However, real particle shape is complex rather than spherical. Parameter identification and energy dissipation, and the dynamical process are mainly considered in most simulations. Relatively less research on deriving a law and mechanism of granular flow impacting a protective structure has been carried out. So, a better and detailed understanding of the dynamics provides a more comprehensive, accurate and reliable basis for the design of protective structures [3].

## Experimental Set-Up

With 2.93m in length, 0.35m in height, and 0.3m in width, the flume was constructed for the experiment of the granular flows (Fig 1A). The flume was able to rotate around a pivot, and a rigid wall was installed perpendicularly to the flume base at the bottom end so that the normal force could be measured. Tested material was limestone gravel with a specific weight of  $13.5\text{kN/m}^3$ , which had particles ranging from 10 to 20mm in diameter. A trigger gate was used to instigate the flow of the material. As shown in Fig 1A,  $L$  was the length, and  $H$  was the height of the initial material, and  $L_1$  was the distance between the trigger gate and the rigid frontal wall obstructing the granular flow. Angle  $\alpha$  was the tilt angle of the flume. The friction angle of the flume base, flume sides (all rigid), and the rigid wall were  $25^\circ$ ,  $15^\circ$  and  $21^\circ$ , respectively [39].

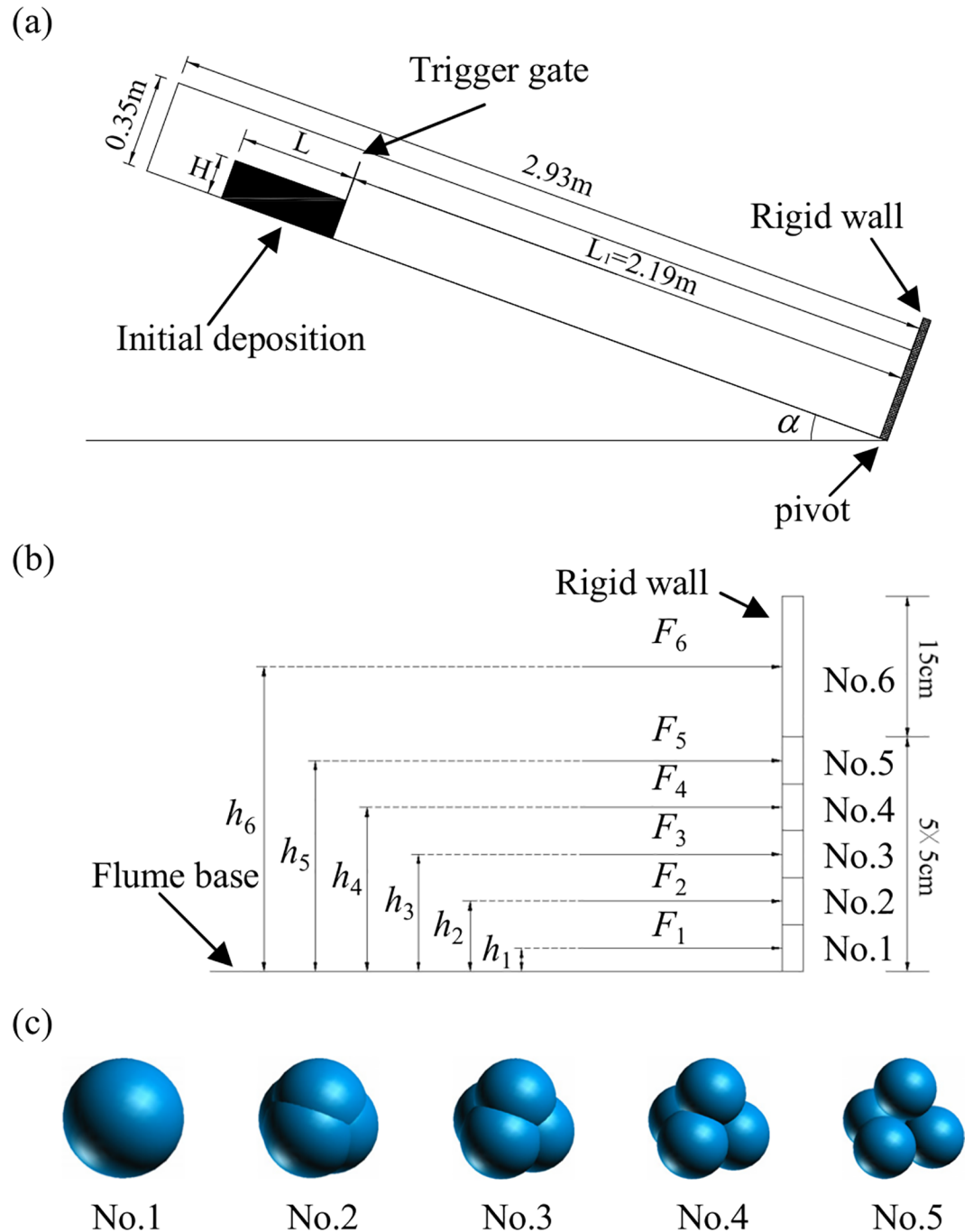


**Fig 1. Experimental equipment.** (a) Sketch of the experimental flume [39] (b) Sketch of the rigid wall (c) Sketch of the clumps

doi:10.1371/journal.pone.0160756.g001

The rigid wall was divided into six segments parallel to the channel slope with a width of 300mm. From the first to the sixth segments, the corresponding normal force of the unit width was designated as  $F_i$ , with  $i$  being the number of each horizontal segments.  $h_i$  was the distance from the centroid of each horizontal segment to the bottom of the rigid wall. As shown in Fig 1B,  $h_1$  to  $h_6$  was 25, 25+50, 25+50+50, 25+50+50+50, 25+50+50+50+50, 25+50+50+50+50+100mm, respectively [39].

## Numerical Modeling

The numerical simulation was carried out using DEM. The spherical element is the basic element in the DEM. Movement and interaction of spherical particles can be modeled directly using DEM. Moreover, it is possible to create clumps with arbitrary shape by attaching two or more particles together. So, it is better to simulate the accumulation and dynamics process of granular flows.

The time step is the calculation cycle of DEM. In every calculation cycle, displacements of each particle can be obtained by repeated application of the law of motion to each particle. Then, contact forces of each particle can be obtained by repeated application of a force-displacement law to each contact which may exist between two balls or between a ball and a wall. The contacts are formed and broken automatically during a calculation cycle.

## Contact-stiffness models

The contact force between two balls or between a ball and a wall [40] is decomposed into a normal component and a shear component. The normal contact force vector is calculated by [40]

$$F_i^n = K^n U^n n_i, \tag{1}$$

where  $K^n$  is the normal stiffness at the contact,  $U^n$  denotes overlap which is defined to be the relative contact displacement in the normal direction and  $n_i$  is a unit normal vector. The shear elastic force-increment vector is calculated by [40]

$$\Delta F_i^s = -K^s U_i^s, \tag{2}$$

where  $K^s$  is the shear stiffness at the contact and  $U_i^s$  is the shear component of the contact displacement-increment vector.

The contact stiffnesses including normal stiffness and shear stiffness relate the contact forces and relative displacements in the normal and shear directions. The common contact-stiffness model is the linear contact model [40] assuming that the stiffnesses of the two contacting entities act in series. The contact normal secant stiffness is calculated by

$$K^n = \frac{k_n^{[A]} k_n^{[B]}}{k_n^{[A]} + k_n^{[B]}}, \tag{3}$$

and the contact shear tangent stiffness is calculated by

$$K^s = \frac{k_s^{[A]} k_s^{[B]}}{k_s^{[A]} + k_s^{[B]}}, \tag{4}$$

where the superscripts [A] and [B] denote the two entities in contact, the  $k_n$  and  $k_s$  are the normal stiffness and shear stiffness of the two entities respectively.

Another contact-stiffness model which is a nonlinear contact formulation is defined by shear modulus  $G$  and Poisson's ratio  $\nu$  of the two contacting balls. The contact normal secant stiffness is calculated by [40]

$$K^n = \left( \frac{2\langle G \rangle \sqrt{2\tilde{R}}}{3(1 - \langle \nu \rangle)} \right) \sqrt{U^n}, \tag{5}$$

and the contact shear tangent stiffness is calculated by [40]

$$K^s = \left( \frac{2\langle G \rangle^2 3(1 - \langle \nu \rangle) \tilde{R}}{2 - \langle \nu \rangle} \right)^{1/3} |F_i^n|^{1/3}, \tag{6}$$

where  $|F_i^n|$  is the magnitude of the normal contact force. For ball-to-ball contact, the multipliers are given by

$$\tilde{R} = \frac{2R^{[A]}R^{[B]}}{R^{[A]} + R^{[B]}}, \tag{7}$$

$$\langle G \rangle = \frac{1}{2}(G^{[A]} + G^{[B]}), \tag{8}$$

$$\langle v \rangle = \frac{1}{2}(v^{[A]} + v^{[B]}), \tag{9}$$

and for ball-to-wall contact, the multipliers are given by  $\tilde{R} = R^{[\text{ball}]}$ ,  $\langle G \rangle = G^{[\text{ball}]}$  and  $\langle v \rangle = v^{[\text{ball}]}$ .

### Clump model

The basic mass properties of a clump are its total mass  $m$ , location of the center of mass  $x_i^{[G]}$ , and moments and products of inertia  $I_{ii}$  and  $I_{ij}$ . For a general clump comprised of  $N_p$  balls, each of which has mass  $m^{[p]}$ , radius  $R^{[p]}$  and centroid location  $x_i^{[p]}$ , the mass properties are defined or calculated by the following equations.

$$m = \sum_{p=1}^{N_p} m^{[p]}, \tag{10}$$

$$x_i^{[G]} = \frac{1}{m} \sum_{p=1}^{N_p} m^{[p]} x_i^{[p]}, \tag{11}$$

$$I_{ii} = \sum_{p=1}^{N_p} \left\{ m^{[p]} (x_j^{[p]} - x_j^{[G]})(x_j^{[p]} - x_j^{[G]}) + \frac{2}{5} m^{[p]} R^{[p]} R^{[p]} \right\}, \tag{12}$$

$$I_{ij} = \sum_{p=1}^{N_p} \left\{ m^{[p]} (x_i^{[p]} - x_i^{[G]})(x_j^{[p]} - x_j^{[G]}) \right\}; \quad (j \neq i), \tag{13}$$

The motion of a clump can be described in terms of the translational and the rotational motion of the entire clump. The equation for rotational motion can be written in the vector form

$$M_i = \dot{H}_i, \tag{14}$$

where  $M_i$  is the resultant moment about the center of mass and  $\dot{H}_i$  is the time rate-of-change of the angular momentum of the clump. The resultant moment is calculated by

$$M_i = \sum_{p=1}^{N_p} \left( \tilde{M}_i^{[p]} + \varepsilon_{ijk} (x_j^{[p]} - x_j^{[G]}) F_k^{[p]} + \sum_{c=1}^{N_c} \varepsilon_{ijk} (x_j^{[c]} - x_j^{[p]}) F_k^{[p,c]} \right), \tag{15}$$

where  $\tilde{M}_i^{[p]}$  is the externally-applied moment acting on particle ( $p$ ),  $F_k^{[p]}$  is the resultant force acting on particle ( $p$ ) at its centroid, and  $F_k^{[p,c]}$  is the force acting on particle ( $p$ ) at contact ( $c$ ).

The clump model was used to carry out the numerical simulations, because it was better to model the real limestone gravel. The clump was comprised of four spherical particles with the

same diameter. At the same time, each distance between two particles within a clump was the same. Compared with the clump comprised of two or three spherical particles, the clump comprised of four spherical particles held spatial characteristics.

As different distance between the two particles within a clump results in different sphericity of the clump, the clump with better sphericity should be selected. The distance between the two particles was designated as  $d$ , and the radius of spherical particles was designated as  $R$ . Five clumps with different sphericity were generated. The relation between  $d$  and  $R$  of the five clumps was  $d = 0$ ,  $d = 0.5R$ ,  $d = R$ ,  $d = 1.5R$  and  $d = 2R$ , respectively. The five clumps which are numbered as 1–5 are shown in Fig 1C, respectively.

In order to calculate the number of clumps needed in the simulations, it is necessary to obtain the quantitative relationship between the volume of a clump and the radius of the spherical particles used in the clump. In clump 1, as  $d = 0$ , the clump was a sphere with the volume calculated by  $4 / 3\pi R^3$ . In clump 5, as  $d = 2R$ , the four spherical particles were tangent to each other. So, the volume of clump 5 was equal to sum of the volume of four spherical particles. However, the calculation formulas of the volume of clump 2, clump 3 and clump 4 were more complex. The volumes of clump2, clump3, clump4, which were obtained using curve fitting method as follows:  $V_2 = 7.4374R^3$ ,  $V_3 = 11.167R^3$ ,  $V_4 = 14.7668R^3$ .

In order to make the volume of the five clumps equal to the volume of the sphere with 20mm in diameter, the radius of spherical particles in each clump should be given as shown in Table 1. At the same time, the specific weight of the clump should be equal to the specific weight of the limestone gravel (taken as 26.5kN/m<sup>3</sup> for the limestone gravel considered). As clump 1 was a sphere, the specific weight of the spherical particles in clump 1 was 26.5kN/m<sup>3</sup>. As the volume of clump 5 was same to the sum of the volume of four spherical particles, the specific weight of the spherical particles in clump 5 was 26.5kN/m<sup>3</sup>, too. However, as shown in Fig 1C, the volume of clump 2, clump 3 and clump 4 was less than the sum of the volume of the four spherical particles, respectively. According to formula (10), the equation of the specific weight  $\gamma$  of spherical particles used in clumps was

$$4 \cdot \frac{4}{3}\pi R^3 \gamma = V_s \gamma_s, \tag{16}$$

where  $V_s$  is the volume of a clump and  $\gamma_s$  is the specific weight of a clump (26.5kN/m<sup>3</sup>). As a result, the specific weight  $\gamma$  of spherical particles used in clumps is shown in Table 1.

Considering that the number of clumps used in the simulations should be similarly equal to the number of material particles in the test, so the number of clumps ( $n_p$ ) is calculated by [41]

$$n_p = \frac{V_t \gamma_t}{V_s \gamma_s}, \tag{17}$$

where  $V_t$  is the total volume of the sample, and  $\gamma_t$  is the specific weight of the sample (13.5kN/m<sup>3</sup>).

**Table 1. Radius and specific weight of spherical particles used in different clumps.**

Clump number	1	2	3	4	5
Radius of spherical particles used in clump(mm)	10	8.3	7.2	6.6	6.3
Specific weight of spherical particles used in clump(kN/m <sup>3</sup> )	26.5	11.8	17.7	23.4	26.5

doi:10.1371/journal.pone.0160756.t001

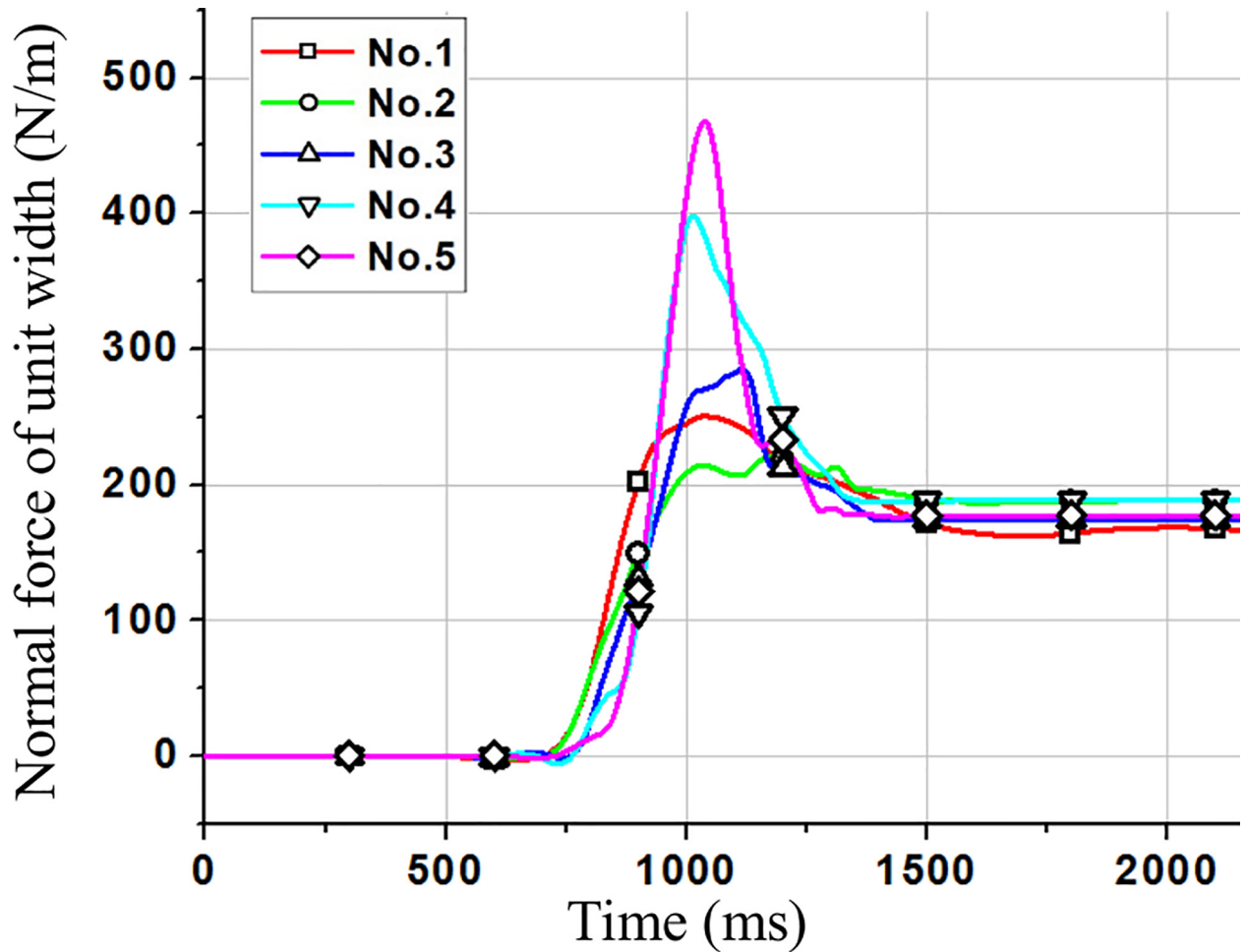


Fig 2. Variation of  $F_1$  with time for the five clumps.

doi:10.1371/journal.pone.0160756.g002

### Numerical Simulation

In the numerical simulation, three different tests including test L34-H15- $\alpha 45^\circ$ , test L44-H20- $\alpha 40^\circ$  and test L44-H15- $\alpha 40^\circ$  were selected for the model calibration and validation. Tested number indicated the condition of the test. For example, L34-H15- $\alpha 45^\circ$  indicated that  $L$  was 34cm;  $H$  was 15cm and  $\alpha$  was  $45^\circ$ .

### Model calibration

In order to select a clump with better sphericity in the five clumps, the numerical simulation for test L34-H15- $\alpha 45^\circ$  was carried out using the five clumps. For the convenience of discussion, the force evolution of  $F_1$  was taken as an example.

Calculation results of residual and peak of  $F_1$  using the five clumps in Fig 2 are shown in Table 2. The residual value and peak value of  $F_1$  were about 190N/m and 350N/m respectively

Table 2. Calculation results of residual and peak of  $F_1$  using the five clumps.

Clump number	1	2	3	4	5
Residual value of $F_1$ (N/m)	167	187	174	189	177
Peak value of $F_1$ (N/m)	251	221	285	398	468

doi:10.1371/journal.pone.0160756.t002

in tests [40]. The calculation results using clump 4 were more close to the experimental data as shown in Table 2. So the clump 4 was selected to complete other numerical simulations.

The calculation results of the time from start to impacting were different from the experimental results. In order to analyze the reason, for test L34-H15- $\alpha 45^\circ$ , the tested material was assumed as a rigid body with the same total volume. According to Newton's second law, the time from start to impacting is 1.1s. However, the frictional resistance of the rigid body is sliding frictional resistance which is more than the frictional resistance of the granular flow in test L34-H15- $\alpha 45^\circ$  (The frictional resistance of the granular flow may be rolling frictional resistance, and the particles in front are pushed at the rear of the granular flow). Therefore, the time of the granular flow from start to impacting was less than the time of the rigid body, which is consistent with the calculation results. As a result, this is reasonable although simulation results of the time were less than experimental results.

## Model validation

According to model calibration, numerical simulations for test L44-H20- $\alpha 40^\circ$  and test L44-H15- $\alpha 40^\circ$  were carried out using clump 4. The simulation results of normal force are shown in Fig 3. Due to the tendency of DEM results showing large fluctuation, de-noising has been carried out on the DEM results for quantitatively comparable to the experimental data.

In test L34-H15- $\alpha 45^\circ$ , the tilt angle of the flume was greater than the tilt angle of the other two flumes. The peak value of  $F_1$  (398N/m) was relatively greater than in the experiment, but with a close residual value in the model (189N/m) compared with the experiment. However, peak and residual value of  $F_4$  in the model were different from experimental values. The residual value of  $F_4$  was greater than the residual values of  $F_2$  and  $F_3$  in the experiment. According to Jiang and Towhata [40], this might be due to a formation of an arch-like protective layer resulting in a non-linear distribution of force with depth. The peak values of  $F_2$ ,  $F_3$ ,  $F_5$  and  $F_6$  in the model were 211, 125, 47 and 30N/m respectively along with peak times 1110, 1255, 1272 and 1328ms respectively. Residual values of  $F_2$ ,  $F_3$ ,  $F_5$  and  $F_6$  were found to be 128, 113, 38 and 26N/m respectively which are all close to the experimental observations.

For test L44-H20- $\alpha 40^\circ$ , the total volume of the sample was greater than the total volume of the samples in the other two experiments. The peak and residual value of  $F_1$  were 484 and 253N/m respectively which are close to the experimental values. The residual value of  $F_2$  (219N/m) was relatively similar to the experiment but with a lower peak value in the model (280N/m) compared with the experiment. For  $F_3$ ,  $F_4$ ,  $F_5$  and  $F_6$ , the peak values captured by the model were 173, 167, 98 and 95N/m at the times 1151, 1283, 1370 and 1283ms, and the residual values were 118, 144, 85 and 72N/m, which are also close to the experimental values.

In test L44-H15- $\alpha 40^\circ$ , the peak values were 416 and 239N/m for  $F_1$  and  $F_2$  respectively which were not similar to the experiment values. Such discrepancy of the force evolution was due to a non-linear distribution of force with depth as discussed in test L34-H15- $\alpha 45^\circ$ . Concerning the rest of the wall, the  $F_3$ ,  $F_4$ ,  $F_5$  and  $F_6$  achieved peak values 149, 93, 70 and 43N/m respectively at the times 1301, 1273, 1323 and 1327ms respectively, and the residual values were 128, 78, 53 and 32N/m which are in relatively good agreement with the experimental results. However, the impact times do not correspond.

According to the comparison results, although calculation results have some differences from experimental data in local details, the simulations of motion process of the granular flow and force evolution of the rigid wall have been carried out in general. In order to investigate the features in the process of flowing, for test L44-H15- $\alpha 40^\circ$ , snapshots of the evolution of simulated flow at several typical moments are shown in Fig 4. Fig 4A showed the accumulation form of the granular flow at the initial moment. Then the granular flow was released

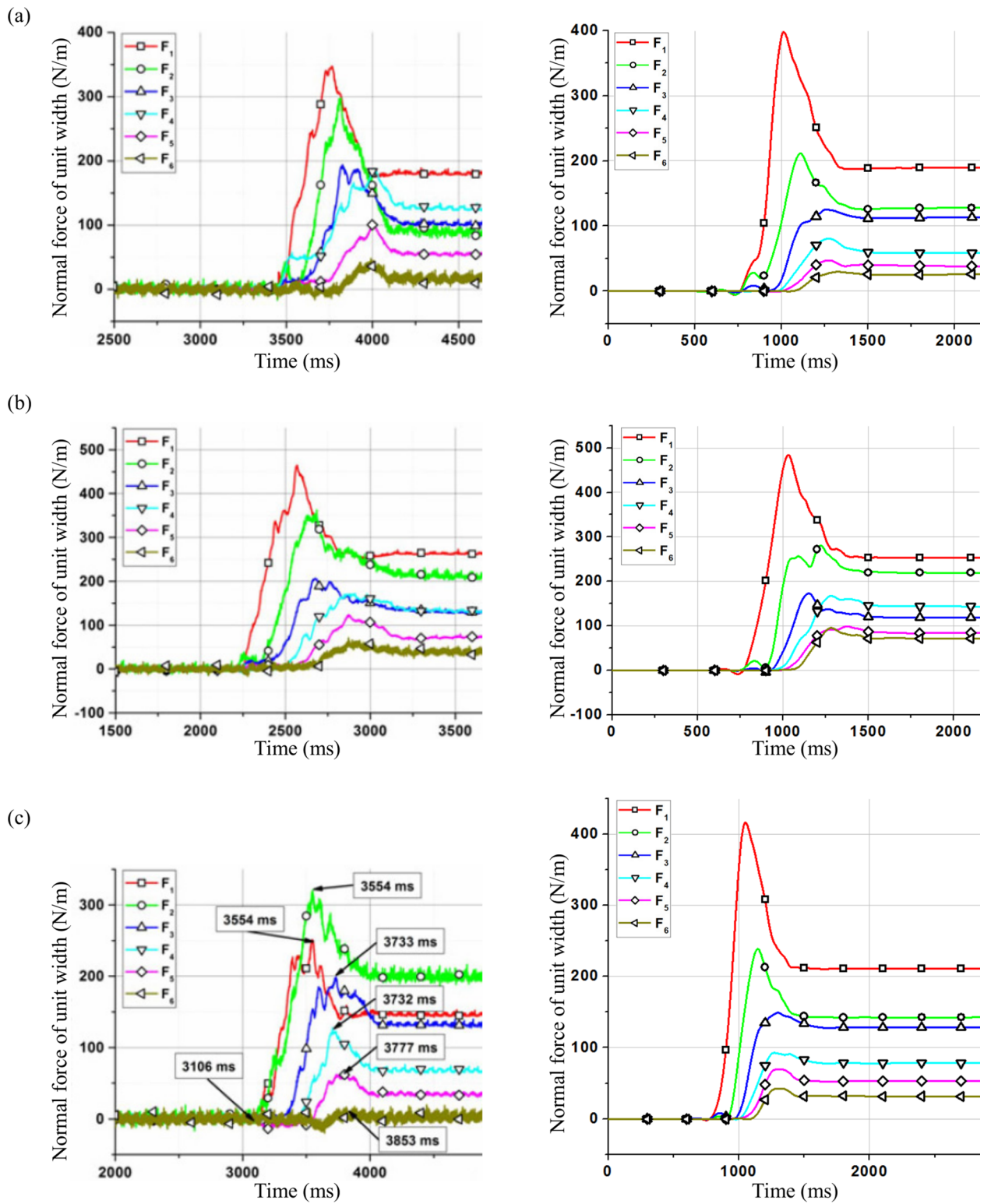


**Fig 3. Time history of normal force variation: experiment [40] and model.**

doi:10.1371/journal.pone.0160756.g003

instantaneously when the trigger gate was taken away. Fig 4B was the calculation result which showed the accelerated development status of the granular flow. The accumulation form of the granular flow was flat and the deformation effect lowered the centre of gravity of the granular flow. In Fig 4C, the granular flow impacted the rigid wall. The particles in the front of the granular flow deposited behind the bottom of the rigid wall after impacting. The particles at back of the granular flow performed upward movement as the particles in front providing a boundary-layer [13]. The shape of the granular flow appeared concave upward. Fig 4D showed the final accumulation form of the granular flow. In the later stage of the motion, due to the embedding of the particles at back of the granular flow and downward movement of the upper unstable particles, the accumulation surface formed a convex shape.

### Total normal force and bending moment

The total force and bending moment acting on the wall were calculated by

$$F = \sum_{i=1}^6 F_i, \tag{18}$$

$$M = \sum_{i=1}^6 F_i h_i, \tag{19}$$

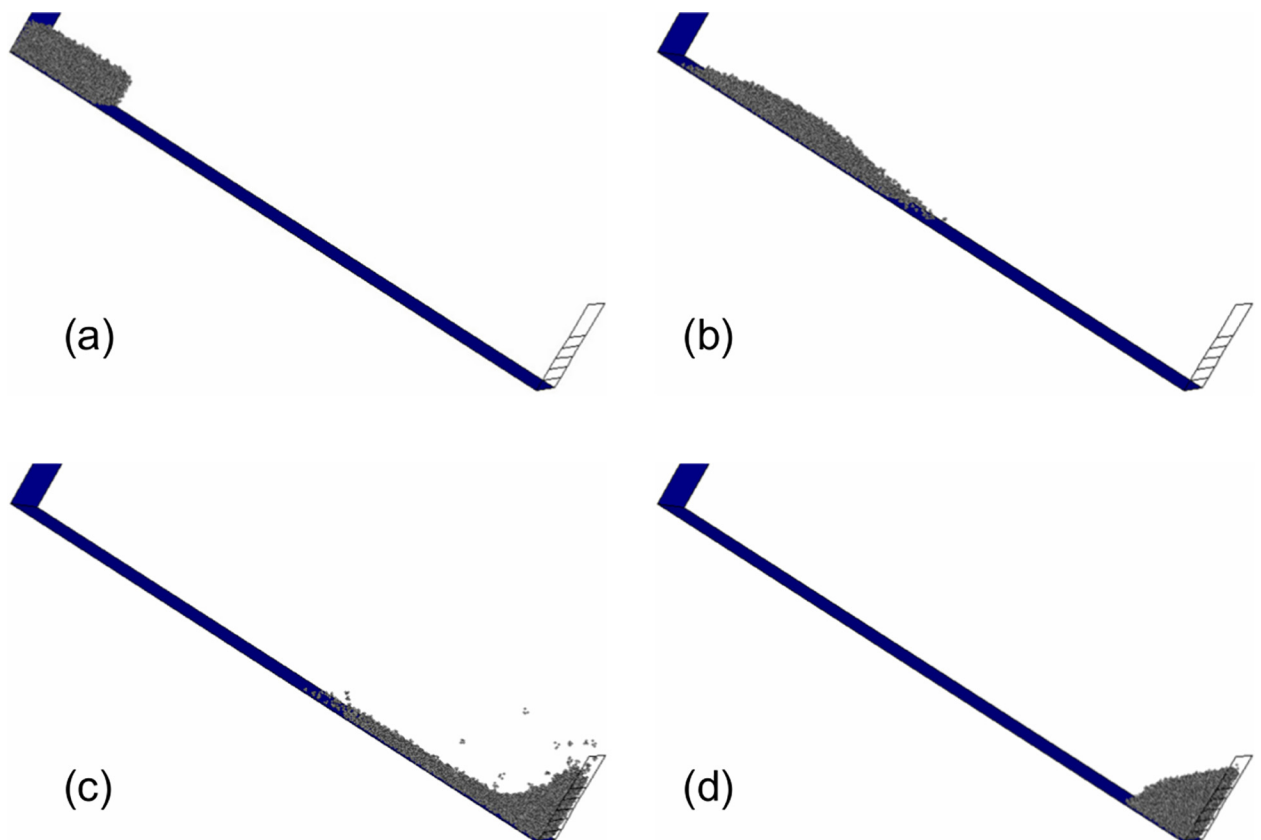


**Fig 4. Snapshots of the evolution of simulated flow through time for test L44-H15-α40°.** (a) at time = 0ms (b) at time = 500ms (c) at time = 1200ms (d) at time = 2300ms

doi:10.1371/journal.pone.0160756.g004

Time history of total normal force and bending moment of experiment and numerical model for test L44-H15- $\alpha 40^\circ$  are shown in Fig 5. The peak and residual value of  $F$  are 807 and 645N/m, respectively, and the peak and residual value of  $M$  are 84 and 68N\*m/m, respectively. All these values fairly agree with the experimental results. However, although the critical times are in good agreements, the absolute impact times do not match.

In general, not only the normal force at each part of the wall, but also the total normal force and bending moment in simulations agree well with experimental results. This verifies the effectiveness of the present model.

### Granular flows with grain composition

In reality, the granular flow is not composed of particles with the same diameter but composed of particles with different grain sizes, called composition. In order to analyze the influence on the force at the rigid wall by grain composition, numerical simulations for test L44-H15- $\alpha 40^\circ$  were carried out using three clumped groups with different simple grain composition. For simplicity, each of clumped groups is assumed to have the same total weight which is equal to the weight of the sample composed of clumps with the same diameter. The mass fractions of clumps with different diameter in three groups are shown in Table 3.

As shown in Fig 6, compared with the calculation results of peak forces using the sample composed of clumps with the same diameter in model validation, the peak values of  $F_1$  and  $F_2$  change obviously. As shown in Table 4, when the particle diameter is not the same, the peak values of  $F_1$  and  $F_2$  are higher. The residual value of  $F_6$  changes which has the same trend with the peak values of  $F_1$  and  $F_2$ . In order to analyze this effect, the distribution of the clumps in the final deposition behind the wall is shown in Fig 7.

As shown in Fig 7, the clumps with larger diameter are mostly distributed at the upper part of the granular flow, such as clumps with 40mm diameter in Fig 7A, 30mm diameter in Fig 7B and clumps with 40mm diameter in Fig 7C. However, compared with the clumps with larger diameter, the clumps with smaller diameter deposit at the bottom of the granular flow. The appearance of particles reverse separation might lead to the change of  $F_6$ . When the particles impact the rigid wall, the impacting of larger clumps causes a greater normal force. This phenomenon is probably caused by the dispersion impact forces of larger clumps, which are

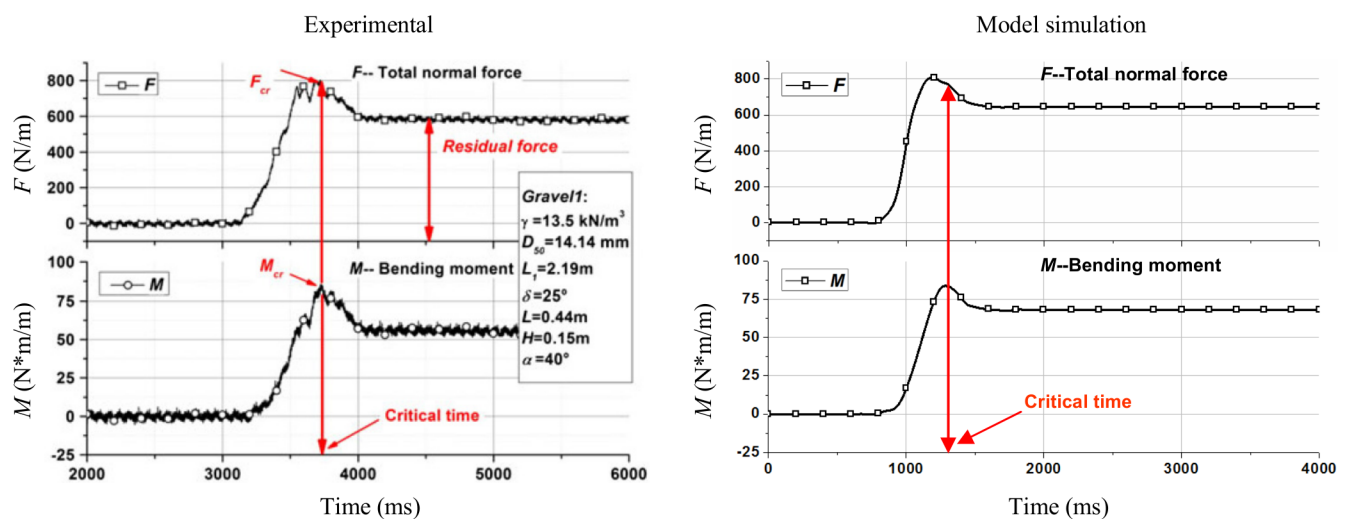


Fig 5. Time history of total normal force and bending moment for test L44-H15- $\alpha 40^\circ$ : experiment [40] and numerical model.

doi:10.1371/journal.pone.0160756.g005

**Table 3. Mass fraction of clumps with different diameter in three groups.**

Clumped group 1					
Diameter(mm)	10		20		40
Mass fraction	25%		50%		25%
Clumped group 2					
Diameter(mm)	15		20		30
Mass fraction	25%		50%		25%
Clumped group 3					
Diameter(mm)	10	15	20	30	40
Mass fraction	5%	20%	50%	20%	5%

doi:10.1371/journal.pone.0160756.t003

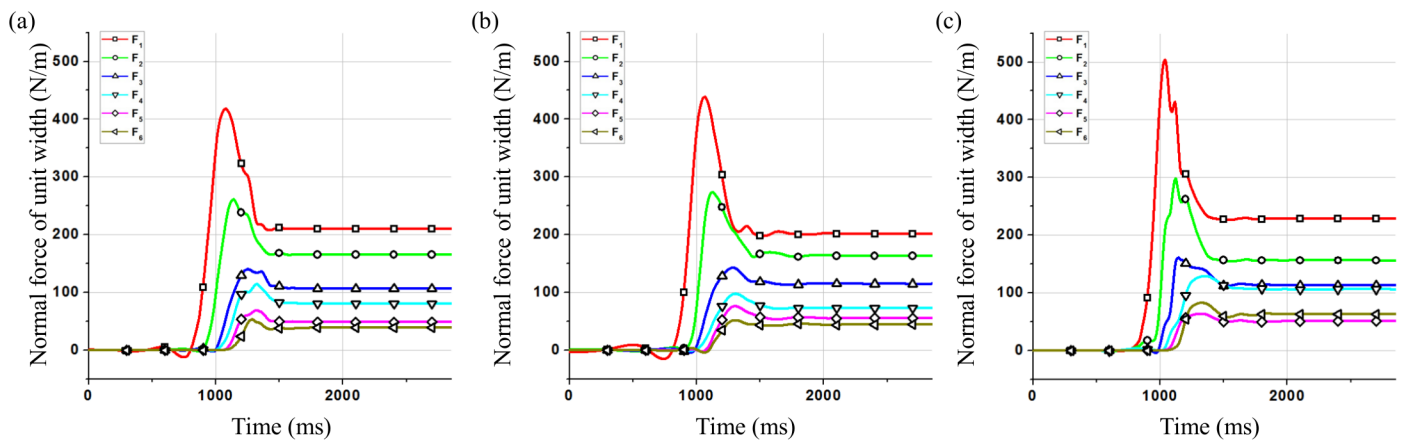


**Fig 6. Time history of normal force of different groups for test L44-H15-α40°.** (a) Clumped group 1 (b) Clumped group 2 (c) Clumped group 3

doi:10.1371/journal.pone.0160756.g006

**Table 4. Calculation results of part of peak and residual values of different groups.**

	clumps with the same diameter	Clumped group 1	Clumped group 2	Clumped group 3
Peak value (N/m) of $F_1$	416	418	438	504
Peak value (N/m) of $F_2$	239	261	274	298
Residual value (N/m) of $F_6$	31	39	44	63

doi:10.1371/journal.pone.0160756.t004

separated reversely to the upper granular flow, while the smaller clumps are mainly concentrated at the bottom of the deposition layer of the granular flow.

Therefore, the grain composition has an effect on the distribution of the force of a rigid wall. For further analysis, numerical simulations for test L44-H15-α40° were carried out using three particle groups with different complex grain composition. The median diameter of the three particle groups were 15, 20 and 25mm. The particle grading curve is shown in Fig 8. Taking into account the influence of computational efficiency, spherical element was used in the simulations. At the same time, numerical simulations were carried out using the particles with the same diameter of 15, 20 and 25mm, respectively.

As shown in Fig 9, calculation results of peak force on the rigid wall become greater when using the particles with complex grain composition than that when using the particles with the same diameter which are the median diameter of the three particle groups. The peak value of the normal force increases when the particle diameter increases, with the most significant increase for  $F_1$ .

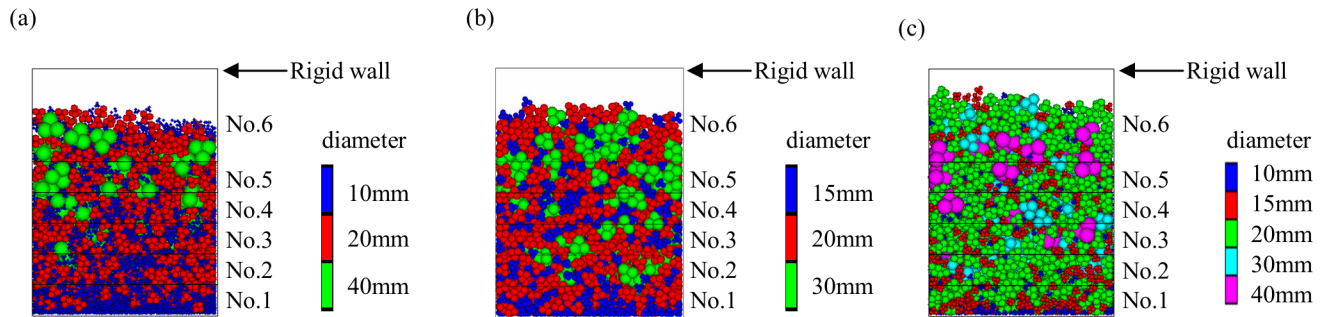


**Fig 7. Distribution of the particles in final deposition behind the wall.** (a) Clumped group 1 (b) Clumped group 2 (c) Clumped group 3

doi:10.1371/journal.pone.0160756.g007

This analysis shows that, the influence of grain composition should be considered on the structural design of the retaining wall, especially at the bottom of the retaining wall. This effectively reduces the potential damage and loss caused by granular flows.

### Conclusions

In this paper, we have carried out numerical simulations of the impact of dry granular flow against a rigid wall using DEM. In the simulations, we have developed a clump model which performs better than spherical ones. Satisfactory agreement has been observed in terms of the normal force of each part of the wall, the total normal force, and bending moment between the model and experiment, which indicates the correctness and effectiveness of the model.

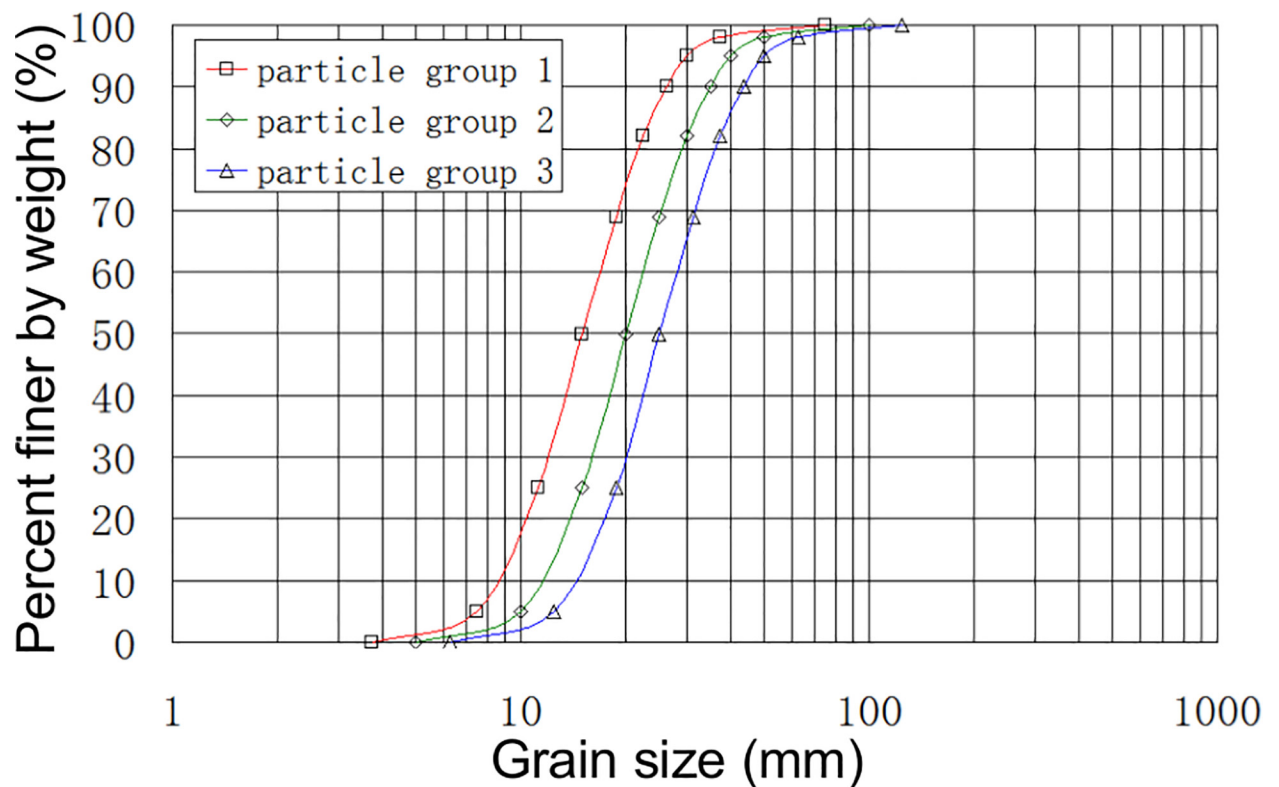


**Fig 8. Particle grading curve.**

doi:10.1371/journal.pone.0160756.g008

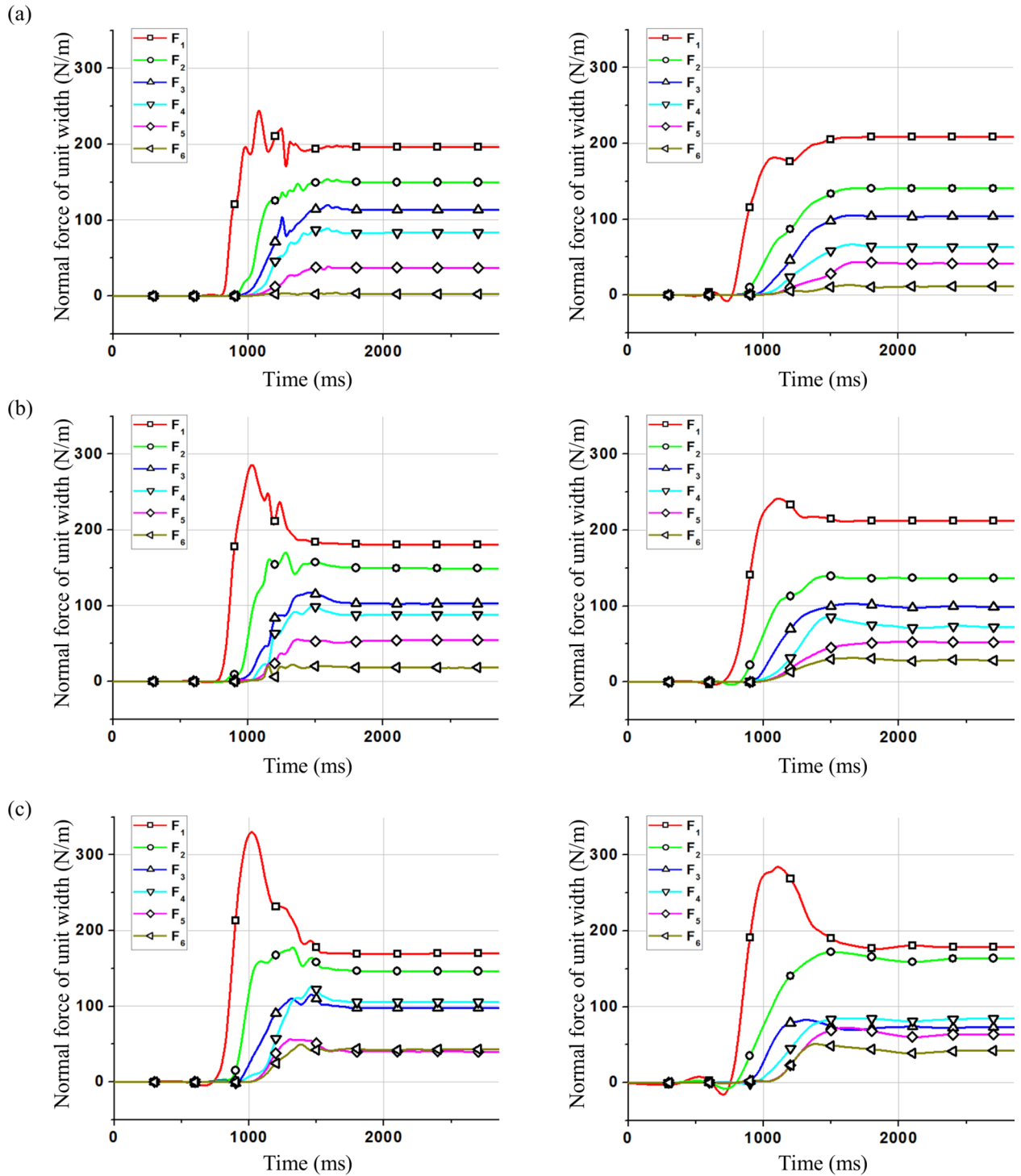


**Fig 9. Calculation results of normal force on the rigid wall using the three particle groups with different complex grain compositions (left) and the particles with the same diameter which are the median diameter of the three particle groups (right).** (a) particle group 1 (b) particle group 2 (c) particle group 3

doi:10.1371/journal.pone.0160756.g009

In the comparison among the calculation results using the groups with different clump diameter and the calculation results using the clumps with the same diameter, it is shown that

the particle diameter distribution is wider, and then the peak force of the wall is greater. This phenomenon is mainly the result of reverse separation in the motion process of the granular flow.

According to the actual grain composition of granular flows, we have carried out the simulation analysis of granular flows with complex grain composition and the particles with the same diameter which is equal to the median diameter. It indicates that the increase of peak force of the wall is due to the increase of particle diameter.

This paper presents the law and mechanism of dry granular flow impacting a rigid wall effectively which promotes the understanding of the granular flow against a retaining structure and provides a reference and basis for the engineering structure design to prevent and mitigate disasters.

## Supporting Information

**S1 File. Data of Fig 2.**

(XLS)

**S2 File. Data of Fig 3.**

(XLS)

**S3 File. Data of Fig 5.**

(XLS)

**S4 File. Data of Fig 6.**

(XLS)

**S5 File. Data of Fig 8.**

(XLS)

**S6 File. Data of Fig 9.**

(XLS)

## Acknowledgments

The authors would like to acknowledge the National Natural Science Foundation of China (Grant No. 41201007, 51474048), the Fundamental Research Funds for the Central Universities (N130401003, L1501009), the Opening Fund of State Key Laboratory of Geohazard Prevention and Geoenvironment Protection of Chengdu University of Technology (Grant No. Sklgp2012K010) and the Research Fund for General Science Project of Department of Education of Liaoning Province (Grant No. L2013103) for the financial support.

## Author Contributions

**Analyzed the data:** LL.

**Contributed reagents/materials/analysis tools:** YF.

**Wrote the paper:** CW.

Contributed to the numerical calculation and simulation: FW.

## References

1. Nikolopoulos EI, Borga M, Creutin JD, Marra F. Estimation of debris flow triggering rainfall: Influence of rain gauge density and interpolation methods. *Geomorphology*. 2015 August 15; 243:40–50.

2. Ouyang C, He S, Tang C. Numerical analysis of dynamics of debris flow over erodible beds in Wenchuan earthquake-induced area. *Engineering Geology*. 2015 August 26; 194:62–72.
3. Pudasaini SP, Hutter K. *Avalanche Dynamics—Dynamics of Rapid Flows of Dense Granular Avalanches*. Springer-Verlag. Berlin. 2007.
4. Pudasaini SP, Miller SA. The hypermobility of huge landslides and avalanches. *Engineering Geology*. 2013; 157:124–132.
5. Lanni C, Mazzorana B, Macconi P, Bertagnolli R. Suitability of mono-and two-phase modeling of debris flows for the assessment of granular debris flow hazards: Insights from a case study. *Engineering Geology for Society and Territory*. 2015 January 4; 2:537–543.
6. Kishi N, Ikeda K, Konno H, Kawase R. In: *Proceedings of Structures under Shock and Impact IV*. 2002:351–360.
7. Manzella I, Labiouse V. Flow experiments with gravel and blocks at small scale to investigate parameters and mechanisms involved in rock avalanches. *Engineering Geology*. 2009; 109:146–158.
8. Azanza E, Chevoir F, Moucheront P. Experimental study of collisional granular flows down an inclined plane. *J Fluid Mech*. 1999; 400:199–227.
9. Faug T, Lachamp P, Naaim M. Experimental investigation on steady granular flows interacting with an obstacle down an inclined channel: study of the dead zone upstream from the obstacle. Application to interaction between dense snow avalanches and defence structures. *Natural Hazards and Earth System Science, Copernicus Publications on behalf of the European*. 2002; 2(3/4):187–191.
10. Hutter K, Koch T. Motion of a granular avalanche in an exponentially curved chute: experiments and theoretical predictions. *Phil Trans R Soc Lond A*. 1991 January 15; 334(1633):93–138.
11. Ancey C. Dry granular flows down an inclined channel: Experimental investigations on the frictional-collisional regime. *Phys Rev E*. 2002; 65:011304.
12. Bi W, Delannay R, Richard P, Valance A. Experimental study of two-dimensional, monodisperse, frictional-collisional granular flows down an inclined chute. *Physics of Fluids*. 2006; 18:123302.
13. Pudasaini SP, Hutter K, Hsiau SS, Tai SC, Wang Y, Katzenbach R. Rapid flow of dry granular materials down inclined chutes impinging on rigid walls. *Physics of Fluids*. 2007; 19(5):053302.
14. Chu T, Hill G., McClung D, Ngun R, Sherkat R. Experiments on granular flows to predict avalanche runup. *Can Geotech J*. 1995; 32(2):285–295.
15. Keller S, Ito Y, Nishimura K. Measurements of the velocity distribution in ping-pong-ball avalanches. *Ann Glaciol*. 1998; 26:259–264.
16. Hanes DM, Walton OR. Simulations and physical measurements of glass spheres flowing down a bumpy incline. *Powder Technology*. 2000; 109:133–144.
17. Dufresne A. Granular flow experiments on the interaction with stationary runout path materials and comparison to rock avalanche events. *Earth Surf Process Landforms*. 2012; 37:1527–1541.
18. Pudasaini SP, Hutter K. Rapid shear flows of dry granular masses down curved and twisted channels. *J Fluid Mech*. 2003; 495:193–208.
19. Savage SB, Hutter K. The motion of a finite mass of granular material down a rough incline. *J Fluid Mech*. 1989; 199:177–215.
20. Iverson RM, Denlinger RP. Flow of variably fluidized granular masses across three-dimensional terrain: 1 Coulomb mixture theory. *Journal of Geophysical Research*. 2001; 106(B1):537–552.
21. Lee BJ. *Continuum simulations of fluidized granular materials*. The University of Texas, Austin 2004.
22. Pudasaini SP. A general two-phase debris flow model. *Journal of Geophysical Research*. 2012; 117: F03010.
23. Domnik B, Pudasaini SP, Katzenbach R, Miller SA. Coupling of full two-dimensional and depth-averaged models for granular flows. *J Non-Newtonian Fluid Mech*. 2013; 201:56–68.
24. Teufelsbauer H, Wang Y, Chiou MC, Wu W. Flow-obstacle interaction in rapid granular avalanches: DEM simulation and comparison with experiment. *Granular Matter*. 2009; 11(4):209–220.
25. Tao H, Jin B, Zhong W, Wang X, Ren B, Zhang Y, et al. Discrete element method modeling of non-spherical granular flow in rectangular hopper. *Chemical Engineering and Processing*. 2010; 49:151–158.
26. Shirsath SS, Padding JT, Kuipers JAM. Numerical investigation of monodisperse granular flow through an inclined rotating chute. *AIChE Journal*. 2014; 60(10):3424–3441.
27. Lee SJ, Hashash YMA. iDEM: An impulse-based discrete element method for fast granular dynamics. *Int J Numer Meth Engng*. 2015; 104:79–103.

28. Maione R, Richter SKD, Mauviel G, Wild G. DEM investigation of granular flow and binary mixture segregation in a rotating tumbler: Influence of particle shape and internal baffles. *Powder Technology*. 2015; 286:732–739.
29. Valentino R, Barla G, Montrasio L. Experimental analysis and micromechanical modelling of dry granular flow and impacts in laboratory flume tests. *Rock Mech Rock Engng*. 2008; 41(1):153–177.
30. Walther JH. Large-scale parallel discrete element simulations of granular flow. *Engineering Computations: International Journal for Computer-Aided Engineering and Software*. 2009; 26(6):688–697.
31. Teufelsbauer H, Wang Y, Pudasaini SP, Borja RI, Wu W. DEM simulation of impact force exerted by granular flow on rigid structures. *Acta Geotechnica*. 2011; 6:119–133.
32. Zhou GGD, Sun QC. Three-dimensional numerical study on flow regimes of dry granular flows by DEM. *Powder Technology*. 2013; 239:115–127.
33. Utili S, Zhao T, Houlsby GT. 3D DEM investigation of granular column collapse: Evaluation of debris motion and its destructive power. *Engineering Geology*. 2015; 186:3–16.
34. Wachs A. A DEM-DLM/FD method for direct numerical simulation of particulate flows: Sedimentation of polygonal isometric particles in a Newtonian fluid with collisions. *Computers & Fluids*. 2009; 38:1608–1628.
35. Neuwirth J, Antonyuk S, Heinrich S, Jacob M. CFD-DEM study and direct measurement of the granular flow in a rotor granulator. *Chemical Engineering Science*. 2013; 86:151–163.
36. Jajcevic D, Siegmann E, Radeke C, Khinast JG. Large-scale CFD-DEM simulations of fluidized granular systems. *Chemical Engineering Science*. 2013; 98:298–310.
37. Li T, Garg R, Galvin J, Pannala S. Open-source MFIx-DEM software for gas-solids flows: Part II-Validation studies. *Powder Technology*. 2012; 220:138–150.
38. Manzella I, Einstein HH, Grasselli G. DEM and FEM/DEM modelling of granular flows to investigate large debris avalanche propagation. *Landslide Science and Practice*. 2013 January 30; 3:247–253.
39. Jiang YJ, Towhata I. Experimental study of dry granular flow and impact behavior against a rigid retaining wall. *Rock Mech Rock Eng*. 2013; 46(4):713–729.
40. Itasca Consulting Group. Inc: PFC3D (Particle Flow Code in 3D) Theory and Background Manual, Version 3.0. ICG, Minneapolis. 2003.
41. Albaba A, Lambert S, Nicot F, Chareyre B. Relation between microstructure and loading applied by a granular flow to a rigid wall using DEM modeling. *Granular Matter*. 2015 October; 17(5):603–616.